Design and Optimization of a 200-kW Medium-Frequency Transformer for Medium-Voltage SiC PV Inverters

Zhicheng Guo, *Student Member, IEEE*, Ruiyang Yu, *Member, IEEE*, Wei Xu, *Student Member, IEEE*, Xianyong Feng, *Member, IEEE*, and Alex Q. Huang, *Fellow, IEEE*

***Abstract*—This article presents a design and optimization methodology for a 200-kW medium-frequency transformer (MFT) based on low-loss magnetic core (FINEMET FT-3TL). The proposed optimal design methodology consists of predesign, preliminary design, and optimal design. In the preliminary design, the parallel-concentric winding structure is selected to increase the current carrying capability and reduce the leakage inductance. Based on the parallel-concentric winding concept, a novel cooing and insulation structure with 3-D printed bobbins are proposed. The optimal designed MFT prototype achieves a power density higher than 19.23 kW/L. The electrical insulation system is tested at 12 kV ac peak voltage. In addition, the partial discharge (PD) test is conducted at 7.5 kV ac peak voltage to ensure the PD-free design. The high-frequency bipolar pulsewidth modulation voltage insulation (PD) test is the first time applied in MFT design and test process. Finally, the transformer is applied in a dual-active-bridge (DAB) converter with 200 kW rated power. The peak efficiency of the DAB converter is 99.53%, and the efficiency at 200 kW is 98.85%. The peak efficiency of MFT is 99.844%, and the efficiency at 200 kW is 99.842%.**

***Index Terms*—Cooing, dual active bridge (DAB), medium-frequency transformer (MFT), optimal design, partial discharge (PD).**

I. INTRODUCTION

TAKING advantage of the superior performance of emerging power semiconductor switches such as SiC MOSFET, photovoltaic (PV) inverters can be designed to connect with medium-voltage (MV) ac grid directly without step-up transformer. Fig. 1 shows the system topology of the proposed MV PV inverter system. Designed to be connected directly to an MV grid at 4.16–13.8 kV or higher, the proposed MV PV inverter utilizes an input-parallel and output-series architecture to achieve the high-output voltage without a line transformer. This will significantly reduce the physical size and weight of the PV inverter system. The dc power is converted to ac by using a dual active bridge (DAB) based isolated dc–dc converter followed by a dc–ac inverter [1]. The dc side is directly connected to the 1500 Vdc PV system, and the peak instant power rating of each converter module is 200 kW.

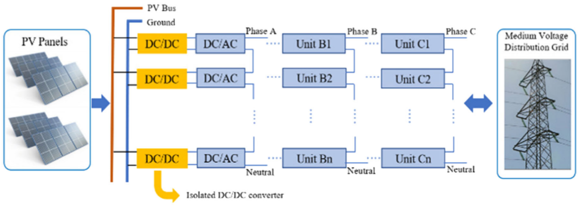

Fig. 1. Block diagram of the proposed MV PV inverter.

The high-power medium-frequency transformer (MFT) is a critical component in the isolated dc–dc converter to achieve high insulation, high power density, and high efficiency. This article discusses the design and optimization of a 200-kW MFT used in the DAB converter.

The primary design challenge for high-power MFTs is to balance the competing objectives including reliable electrical insulation, high efficiency, high power density, and the superior thermal performance [2]–[7]. Some existing high-power MFTs are summarized in Table I. These designs have power rating exceeding 50 kW, and the operating frequency is in the range of 1.75–22 kHz [8]–[14]. Amorphous, ferrite, and nanocrystalline are typical magnetic core materials for MFTs. Liquid cooling, heatsink cooling, and air cooling are most popular cooling methods used in MFTs.

The designs in [9] and [10] present two transformers for 166 kW/20 kHz based on two different core materials. Ferrite and nanocrystalline-based MF transformers differ in cooling system design, and ultimately in power density. The CUT [11] also introduces two MFT prototypes (50 kW/5 kHz) design by using nanocrystalline and ferrite magnetic cores, respectively. Test results suggest that the nanocrystalline core MFT has a higher power density and efficiency. However, there is no comparison study to report the MFT performance difference using different winding structures with the same magnetic core. In addition, the partial discharge (PD) behavior and insulation

---

Manuscript received May 18, 2020; revised September 2, 2020 and December 8, 2020; accepted February 5, 2021. Date of publication February 17, 2021; date of current version June 1, 2021. This work was supported by the U.S. Department of Energy's Office of Energy Efficiency and Renewable Energy (EERE) under Solar Energy Technologies Office (SETO) Agreement EE0008348. Recommended for publication by Associate Editor Q. Li. *(Corresponding author: Ruiyang Yu.)*

The authors are with the Semiconductor Power Electronics Center, The University of Texas at Austin, Austin, TX 78712 USA (e-mail: zcguo@utexas.edu; ryanyu@utexas.edu; wei.xu@utexas.edu; x.feng@cem.utexas.edu; aqhuang@utexas.edu).

Color versions of one or more figures in this article are available at https://doi.org/10.1109/TPEL.2021.3059879.

Digital Object Identifier 10.1109/TPEL.2021.3059879

TABLE I
SUMMARY OF HIGH-POWER MFTS AND THE MFT REPORT IN THIS ARTICLE

	Power Rating (kW)	Frequency (kHz)	Magnetic Core Material	Cooling Method	Insulation Voltage (kV)	Efficiency %	Power Density kW/L	Apply High-frequency insulation PD test in design
ABB 2011 [8]	150	1.75	Nanocrystalline	Oil	15	96%	N/A	N/A
ETH 2013 [9,10]	166	20	Nanocrystalline Ferrite	Water Air	N/A	99.5% 99.4%	32.7 8.21	N/A
CUT 2016 [11]	50	5	Nanocrystalline Ferrite	Air cooled heatsink	6	99.66% 99.58%	15 11.5	N/A
EPFL 2017 [12]	100	10	Nanocrystalline	Air cooled heatsink	>6	99.3%	8.2	N/A
ABB 2017 [13]	240	10	Nanocrystalline	Air	PD (35kV)	99.23%	3.6	N/A
ABB CERN 2017 [14]	100	15kHz-22kHz	Nanocrystalline	Air Oil	PD (30kV)	99.5%	1.1	N/A
UT Austin [This work]	200	15kHz	Nanocrystalline	Air	13 kV PDIV (5kV)	99.842%	>19.23	YES

performance of MFT are not extensively investigated in some previous designs. Especially, PD behavior under high-frequency bipolar pulsewidth modulation (PWM) waveforms has not been discussed and applied to MFT insulation design. Electrical insulation is very important for MV applications to ensure the reliability and lifetime of MFT. ABB [8], [13], [14] presents the PD test for their MFTs at 38, 35, and 30 kV to prove the design, but no detailed optimal design for electric field distribution under bipolar PWM excitation is discussed.

Previous research [11], [12], [15], [16] investigated the optimal design methodologies for MFTs. The methodologies have the aim of reaching the best MF transformer for a given power converter topology, by optimizing transformer efficiency, weight, transformer leakage, and magnetizing inductances at the same time. Still lot of challenges due to lack of sufficient flexibility and effectivity due to the restriction of the commercial cores and Litz wire products.

This article proposes a comprehensive optimal design methodology consisting of predesign, preliminary design, and optimal design. Leveraging the advantage of 3-D print technology, more optimal design freedoms and accurate fabrication can be achieved. As part of the preliminary design, an optimal winding structure of MFT is selected based on a comprehensive comparison study among various potential structures in terms of magnetizing inductance, leakage inductance, window utilization, thermal behavior, insulation performance, and power density.

Moreover, a new insulation structure is proposed with 3-D printed bobbins for the selected winding structure. To my knowledge, the proposed MFT is the first design which applies high-frequency bipolar PWM voltage insulation (PD) test in the design process and verification. The air channels are intentionally introduced in the 3-D printed bobbins to improve the heat dissipation of the core and inner-layer windings. Finally, the optimal design is conducted with FEA simulation and engineering calculation. At last, the prototype of the final optimal design is verified by experimental tests. The MFT efficiency is 99.842%, and the temperature rise is lower than 30 °C at 200 kW. At this power level, the calculated power density is 19.23 kW/L.

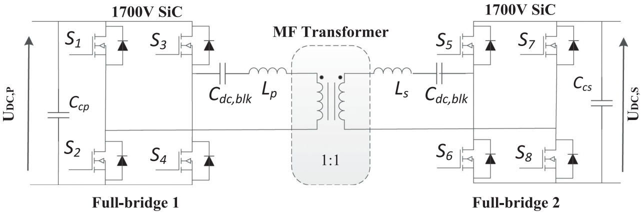

Fig. 2. Circuit diagram of DAB.

TABLE II
SPECIFICATIONS OF THE HIGH-POWER MFT

Parameter	Value
Power rating	200 kW
Input/output voltage	1300 V
Primary/secondary RMS current	150 A
Working frequency (fs)	15 kHz
Transformer turn ratio	1:1

The rest of this article is organized as follows. Section II describes the DAB converter topology and the MFT specifications. In Section III, the design process is discussed, including magnetic core and Litz wire selection, winding structure comparison, losses evaluation, cooling considerations, and insulation design. Section IV proposes the optimization methodology based on the design procedures mentioned in Section III. Section V presents the PD and efficiency test results as well as the thermal performance of the MFT at 200 kW. Finally, the conclusion is given in Section VI.

II. CONVERTER TOPOLOGY

The DAB is one of the most commonly used topologies for isolated dc–dc converters [17]–[19], as shown in Fig. 2. It consists of two 1700-V SiC MOSFET-based full-bridges, a 1:1 MFT providing the galvanic isolation, two external 14 μH inductors and two dc blocking capacitors. The selected working frequency of the MFT is 15 kHz, which is based on the efficiency and dimension optimization of the whole DAB converter system [20] and [21]. The designed MFT specifications are summarized in Table II.

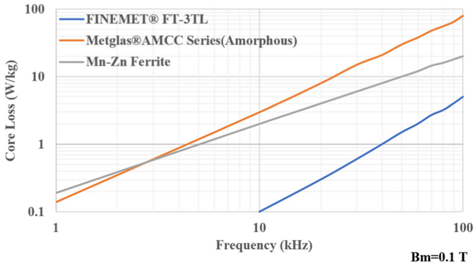

Fig. 3. Soft magnetic materials core loss comparison.

TABLE III
PARAMETERS OF THE SELECTED MAGNETIC CORE AND LITZ WIRE

<table>
<tr><th colspan="5">Core Parameters</th><th>Core Diagram</th></tr>
<tr><td>A
(mm)</td><td>B
(mm)</td><td>C
(mm)</td><td>D
(mm)</td><td>E
(mm)</td><td rowspan="4">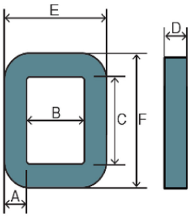 </td></tr>
<tr><td>50</td><td>60</td><td>140</td><td>30</td><td>180</td></tr>
<tr><td>F
(mm)</td><td>Ae
(mm2)</td><td>Lm
(mm)</td><td>Weight
(kg)</td><td>Pe*1(W Max)@20 kHz 0.1T</td></tr>
<tr><td>240</td><td>1125</td><td>575</td><td>4.7</td><td>2.8</td></tr>
<tr><th colspan="5">Litz Wire Parameters</th><th>Litz wire Diagram</th></tr>
<tr><td>Width/ Thickness</td><td>Conductor resistance max.ohm/km @20℃</td><td>Stand number /AWG</td><td colspan="2">Twisted Breakdown Voltage Test 9 cycle (AC)</td><td rowspan="2"></td></tr>
<tr><td>8.0mm± 0.2/ 6.8mm ±0.2</td><td>0.97Ω/kM</td><td>4000/40</td><td colspan="2">3.00kv</td></tr>
</table>

III. MFT DESIGN PROCEDURE

A. *Magnetic Core and Litz Wire Selection*

Soft magnetic materials with high saturation flux density, low specific core losses, and excellent thermal and mechanical properties are considered as a perfect choice for this type of application. In most cases, it is hard to find a soft magnetic material with all performances superior to the others, so tradeoffs need to be considered [22]–[24]. The core loss density of three types of common magnetic core materials is compared in Fig. 3. It shows that FINEMET FT-3TL holds the lowest core loss density up to 100 kHz. Also, FINEMET FT-3TL has higher saturation flux density (1.2 T) as compared with Mn–Zn Ferrite material cores. Besides, FINEMET FT-3TL material core with suitable geometry is commercially available. The selected core geometry parameters are listed in Table III [25]. Considering vibration and acoustic noise issues, the nanocrystalline uncut core is the best selection for medium-frequency high-power application [26]. To increase the core cross-section area, two identical cores are stacked together for the 200 kW MFT construction. The required core dimensions can be roughly estimated by using the product areas (A_p) method [27]

$$A_p \approx \frac{P}{K_f K_u B_m f J}. \tag{1}$$

Rectangular Litz wire with 4000 strands/AWG40 was customized design since it reduces eddy current losses and improves the window utilization factor. Considering the transformer windings have lower ac resistance at wider frequency range, AWG40 Litz wire is selected.

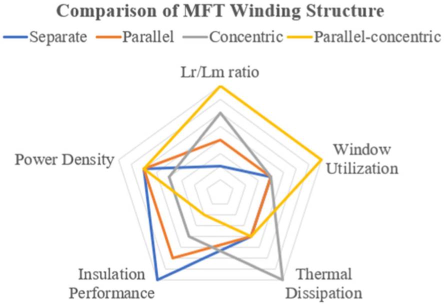

Fig. 4. Comparison of MFT winding structure.

B. *Parallel-Concentric Winding Structure*

In addition to winding loss and core loss, the nanocrystalline magnetic material is sensitive to eddy current losses, which induces by leakage inductance [28]. The low-leakage inductance of MFT improves efficiency and reduces the hotspot temperature in the core. Fig. 4 and Table IV compare the performance of four different MFT winding structures based on the design requirements of the high-power MFT and the selected magnetic core. The separate winding structure means the primary winding and secondary winding are separated to different limbs of the core. The parallel winding structure represents the primary side, and secondary side is divided into two equal parallel parts winding at two core limbs. In the concentric structure MFT, the secondary winding surrounds the primary side only in the middle of the limb formed by the two cores. For the parallel-concentric winding structure, the primary side and the secondary side windings are divided into two equal parallel parts. Two primary side windings surround the transformer core legs, and two secondary side windings surround two primary side windings.

The parallel-concentric winding structure has the best coupling between the primary and secondary windings and consequently obtains the lowest leakage inductance.

The measured results show the MFT with separate winding structure has the largest leakage inductance of 59 μH. In contrast, the parallel-concentric winding structure has the lowest leakage inductance of 2.6 μH and lowest leakage inductance to magnetizing inductance ratio (0.023%). Besides, the parallel-concentric winding structure also improves the window area utilization factor. In this way, the winding conductor resistance decreases, which is very important for high-power applications. The concentric winding structure has the best thermal dissipation performance because of the largest exposed surface area. For insulation design, the separate winding structure has more flexibility, while the parallel-concentric structure is limited by the well-coupled windings and high window area utilization. To achieve high efficiency and high-power-density, the parallel-concentric winding structure is selected for further optimization. To address the weakness in the thermal behavior and electrical insulation, a novel 3-D printed structure for the MFT is proposed and will be discussed in a later section.

TABLE IV
COMPARISON OF TWO CORES MFT STRUCTURES

	Separate	Parallel	Concentric	Parallel-Concentric
Turns ratio: 10:10 Frequency: 15 kHz	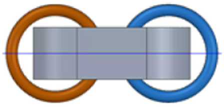	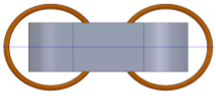	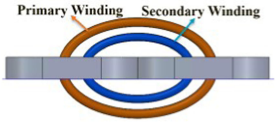	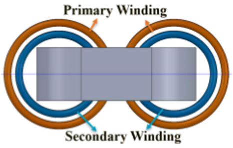
	Top view	Top view	Top view	Top view
	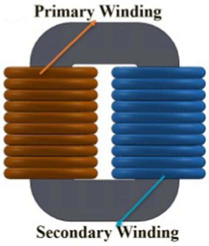	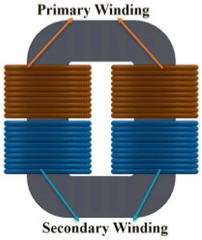	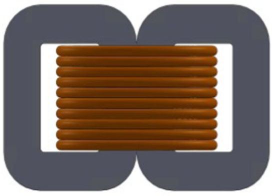	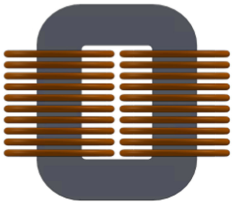
	Front view	Front view	Front view	Front view
Magnetizing Inductance	11.02 mH	11.03 mH	11.02 mH	11.01 mH
Leakage Inductance	59 µH	15 µH	4 µH	2.6 µH
Window Utilization	Fair (**)	Fair (**)	Fair (**)	Best (****)
Thermal Dissipation	Fair (**)	Fair (**)	Best (****)	Fair (**)
Insulation Performance	Best (****)	Good (***)	Fair (**)	Bad (*)
Power Density	Good (***)	Good (***)	Fair (**)	Good (***)

TABLE V
CORE LOSS EVALUATION MODEL EXPRESSIONS

OSE	$P_v = Kf^{\alpha}B_m^{\beta}$
MSE	$P_v = Kf_{eq}^{\alpha-1}B_m^{\beta}$ $f_{eq} = \dfrac{2}{\Delta B^2\pi^2}\int_0^T \left(\dfrac{dB(t)}{dt}\right)^2 dt$
GSE	$P_v = \dfrac{1}{T}\int_0^T k_1\left\lvert\dfrac{dB(t)}{dt}\right\rvert^{\alpha}\lvert B(t)\rvert^{\beta-\alpha}\,dt$ $k_1 = \dfrac{K}{(2\pi)^{\alpha-1}\int_0^{2\pi}\lvert\cos\theta\rvert^{\alpha}\lvert\sin\theta\rvert^{\beta-\alpha}d\theta}$
IGSE	$P_v = \dfrac{1}{T}\int_0^T k_i\left\lvert\dfrac{dB(t)}{dt}\right\rvert^{\alpha}\lvert B(t)\rvert^{\beta-\alpha}\,dt$ $k_i = \dfrac{K}{(2\pi)^{\alpha-1}\int_0^{2\pi}\lvert\cos\theta\rvert^{\alpha}2^{\beta-\alpha}d\theta}$

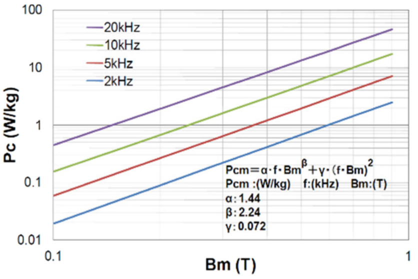

Fig. 5. Core loss density approximation of large size FINEMET noncut core with insulation layer.

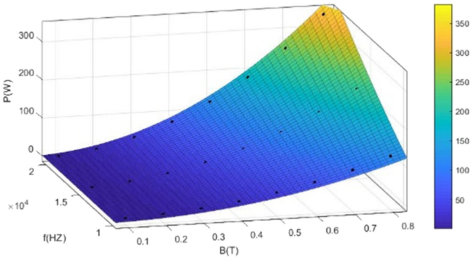

Fig. 6. Core losses versus frequency f and flux density B for two cores.

C. Core Loss Evaluation

Generally, hysteresis models, loss separation approach, and empirical methods can conduct magnetic loss evaluation [29]. The original Steinmetz equation (OSE) [30] is only valid for sinusoidal excitation waveforms. In [31], a modified Steinmetz equation (MSE) is developed to estimate core loss with nonsinusoidal waveforms. Generalized Steinmetz equation (GSE) [32] refines the hypothesis of how loss depends on (dB/dt). To take the time history of magnetic material into account, the improved GSE (IGSE) [33] model is proposed. The calculated expressions for each of the previously mentioned methods are listed in Table V.

Fig. 5 shows the core loss density approximation of FINEMET noncut core. Based on the core loss density data from 10 to 20 kHz, a 3-D curve of core loss versus frequency f and flux density B can be visualized in Fig. 6. A curve fitting expression of measured data is derived using the OSE. Thus, all the specific core loss calculation expressions in Table V can be estimated, where K, α, and β are determined by the magnetic core characteristics, f is the frequency of the excitation waveform, and ΔB is the peak-to-peak magnetic induction.

The transformer voltage and magnetic induction waveforms of a typical DAB converter with single-phase shift degree θ are shown in Fig. 7.

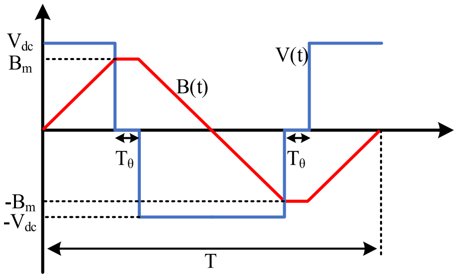

Fig. 7. Typical DAB MFT voltage waveform and magnetic induction with a phase shift θ.

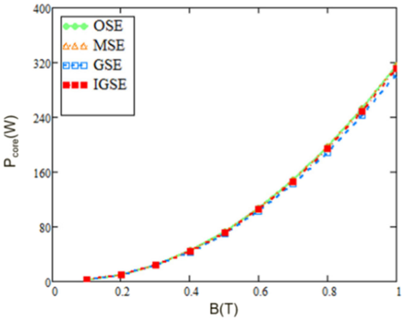

Fig. 8. Core loss models comparison for two stacked FINEMET FT-3TL cores, with $\alpha = 1.449, \beta = 2.12, K = 0.245$, and $f = 15$ kHz.

The core loss evaluation model is summarized in Table V. Based on the characteristic waveform as shown in Fig. 7, the analysis can be divided into four stages

$$\left|\frac{dB(t)}{dt}\right| = \begin{cases} \frac{2\Delta B}{DT}, \; 0 < t < \frac{T}{2} - T_\theta \\ 0, \frac{T}{2} - T_\theta < t < \frac{T}{2} \\ \frac{2\Delta B}{DT}, \frac{T}{2} < t < T - T_\theta \\ 0, T - T_\theta < t < T \end{cases} \tag{2}$$

where D is the duty ratio of the voltage waveform and T_θ is the phase-shift time.

Fig. 8 presents the core loss estimation results using OSE, MSE, GSE, and IGSE methods. The comparison results indicate that these methods can obtain consistent results for core losses estimation. Finally, the IGSE method is selected as the core loss evaluation model because of it has been verified copes better with a wider variety of voltage waveforms.

D. Windings Loss Evaluation

MFT winding losses depend on the transformer current and winding ac resistance. To estimate the frequency-dependent winding losses, accurate ac winding resistance, and corresponding harmonic current is required. The original Dowell's model [34], [35] provides a frequency-dependent expression to estimate winding resistance factor F_r for solid wire and foil. Fig. 9 shows the structure of rectangular Litz wire winding and equivalent foil winding. The ac–dc resistance ratio F_r can be written as

$$F_r = \sqrt{\eta}\,\varsigma\left(\psi_1(\varsigma) + \frac{2}{3}\left(m^2 - 1\right)\psi_2(\varsigma)\right) \tag{3}$$

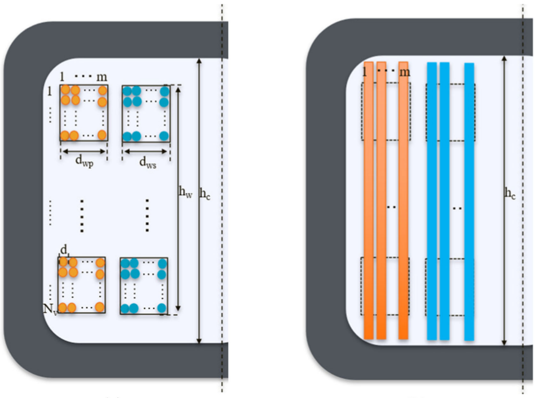

(a) (b)

Fig. 9. Structure of equivalent winding. (a) Rectangular Litz wire winding. (b) Equivalent foil winding.

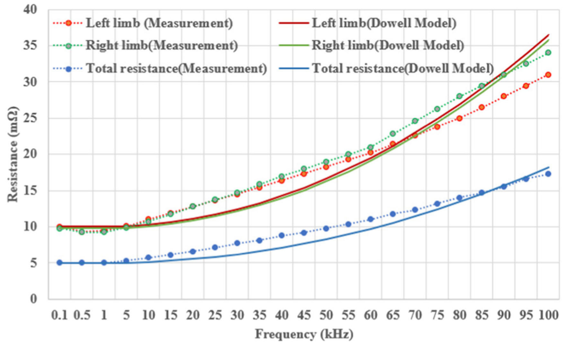

Fig. 10. Plots of transformer prototypes winding ac resistance.

where the skin effect factor $\psi_1(\varsigma)$ and proximity effect factor $\psi_2(\varsigma)$ are defined as follows:

$$\psi_1(\varsigma) = \frac{\sinh 2\varsigma + \sin 2\varsigma}{\cosh 2\varsigma - \cos 2\varsigma} \tag{4}$$

$$\psi_2(\varsigma) = \frac{\sinh \varsigma - \sin \varsigma}{\cosh \varsigma + \cos \varsigma} \tag{5}$$

where the equivalent penetration ratio ς, porosity factor η, and equivalent thickness of foil d_{eq} are defined as

$$\varsigma = \frac{d_{\mathrm{eq}}}{\delta} \tag{6}$$

$$\eta = \frac{h_w}{h_c} \tag{7}$$

$$d_{\mathrm{eq}} = d\sqrt{\frac{\pi}{4}} \tag{8}$$

where m is the number or layers, h_w is the height of the layer, h_c is the core window height, δ is the skin depth the thickness of the foil, and d is diameter of Litz wire.

Fig. 10 shows the comparison results between winding resistance measurement value using Hioki IM3536 LCR meter and Dowell model estimation value. The error is within the acceptable range. Besides, the current sharing of the parallel windings is good especially at lower frequency range. To calculate the winding loss for nonsinusoidal current waveform, fast Fourier transform (FFT) is applied to the current waveform. The total

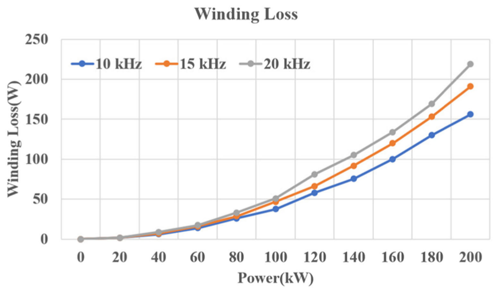

Fig. 11. MFT winding losses for different operating frequency (10, 15, and 20 kHz).

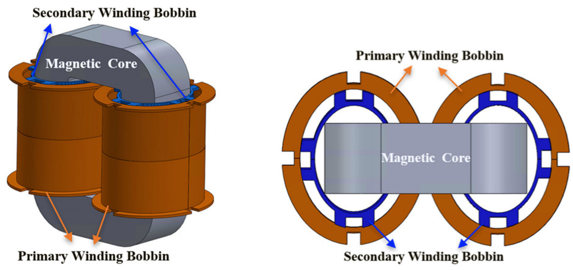

(a) (b)

Fig. 12. 3-D printed two layers bobbin design. (a) 3-D view. (b) Top view.

losses can be calculated as the sum of the loss at each sine wave frequency [36], [37], as shown in the following equation:

$$P_{\text{winding}} = \sum_{n=1}^{13} I_{\text{RMS}}(n)^2 R_{\text{AC}}(n) \tag{9}$$

where n is the FFT component index, $R_{\text{AC}}(n)$ is the winding resistance at the nth frequency range, $I_{\text{RMS}}(n)$ is the current component at the nth frequency range, which is equal to $\text{FFT}_{\text{magnitude}}(n)/\sqrt{2}$. The number of harmonics is up to 13 due to the ignorable current at higher order.

Fig. 11 shows the calculated winding losses at operating frequency at 10 kHz, 15 kHz, and 20 kHz. As the power level increase from 0 to 200 kW, the winding losses increase significantly. With higher operating frequency, the ac winding resistance is higher which results in higher winding losses at the same out power.

E. Cooling Considerations

The thermal performance is another major consideration for high-power MFT. The operating temperature determines the lifetime and reliability of MFT. The cooling system design is a challenge for this 200-kW high-power-density MFTs. To achieve the superior cooling performance, a novel cooling structure is proposed which utilizes two layers 3-D printed bobbins, as shown in Fig. 12. The 3-D printed structure can provide airflow channels for the core and windings.

To illustrate the effectiveness of the proposed cooling system, a detailed thermal network of MFT is constructed, which consists of conduction, convection, and radiation thermal resistances. Due to the symmetric structure of the MFT prototype, one part of whole MFT structure is elaborated in Fig. 13. For the

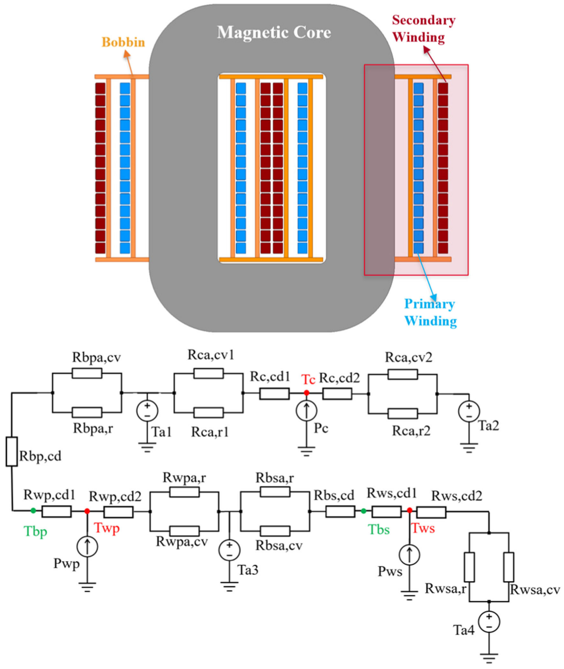

Fig. 13. Detailed steady-state thermal network model of the MFT based on conduction, convection, and radiation thermal resistances.

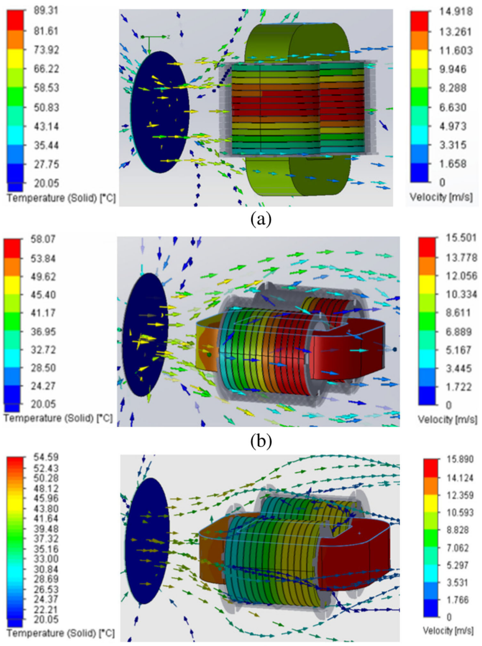

(a)

(b)

(c)

Fig. 14. Fluid thermal simulation of different cooling structure under 15 m/s airflow speed. (a) Standing core with air channels bobbin. (b) Lay core without air channels bobbin. (c) Lay core with air channels bobbin.

proposed cooling system, the outer-layer windings are simplified as convection flow over plate heat transfer and inner windings are simplified as convection internal flow heat transfer, as listed in Table VI [38], [39].

Fig. 14 compares the temperature rises of three cooling structures under 15 m/s airflow speed condition. To match the real

TABLE VI
HEAT TRANSFER TYPES FOR THE PROPOSED COOLING SYSTEM

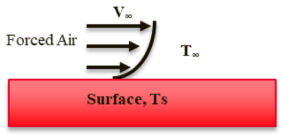 Convection Flow over plates	Laminar boundary layer: $N_u = 0.664 R_e^{\frac{1}{2}} P_r^{\frac{1}{3}}$	$Q_{conv} = h_c A(T_s - T_\infty)$, $h_c = \frac{N_u k}{L}$
	Turbulent boundary layer: $N_u = 0.037 R_e^{\frac{4}{5}} P_r^{\frac{1}{3}}$	
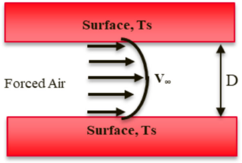 Convection Internal flow	Laminar flow, entrance region : $N_u = 1.86 \left(\frac{R_e P_r}{L/D}\right)^{\frac{1}{3}} \left(\frac{u_b}{u_w}\right)^{0.14}$	
	Laminar flow, fully developed: $N_u = 3.66$	
	Turbulent Flow, fully developed: $N_u = 0.023 R_e^{\frac{4}{5}} P_r^{0.3}$	
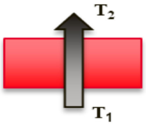	Conduction	$Q_{cond} = kA\frac{\partial T}{\partial x}$
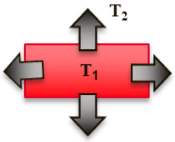	Radiation	$Q_r = h_r A \Delta T$, $h_r \approx 4\sigma\varepsilon T_{avg}^3$

where h: heat transfer coefficient Reynolds number: R_e Prandtl number: P_r Nusselt number: Nu σ is the Stefan–Boltzmann constant ε is the emissivity of the radiative surface k thermal conductivity.

test situations, the ambient temperature is settled as 25 °C in all thermal simulations. The results show that the lay core with air channels bobbin design has the best heat dissipation performance. The 3-D fluid simulation shows the MFT hotspot temperature is around 54 °C, which matches well with the experimental results, as shown in Fig. 26. For the parallel-concentric winding structure, the inner-layer winding always has higher temperature because the inner layer is surrounded by outer-layer winding as an external heat source. So, the temperature of the inner-layer winding and core is monitored in the simulation. Fig. 15 presents a sensitivity analysis results for the three cooling structures with various airflow speeds. Fig. 15(a) shows the flat lay with air-channel bobbin design has the lowest core temperature rise with airflow speed range from 2 to 20 m/s. The temperature rise difference among the three structures are not significant due to the high thermal conductivity of core material. The advantages of proposed cooling design are reflected in inner winding temperature control, as shown in Fig. 15(b). The thermal simulation results indicate that lay core with air channel cooling structure achieves the lowest temperature difference between core and inner winding as well as the lowest temperature rise at all airflow speeds.

Based on the losses evaluation models and cooling system mentioned above, Fig. 16 shows the MFT efficiency and hotspot temperature at power rating up to 400 kW. MFT core temperature is around 55 °C , which higher than windings temperature when power rating lower than 220 kW. Then, winding temperature rises rapidly at higher power rating due to the increase of winding loss. Considering materials properties and reliability, the MFT can provide 340 kW out power with steady-state temperature lower than 100 °C.

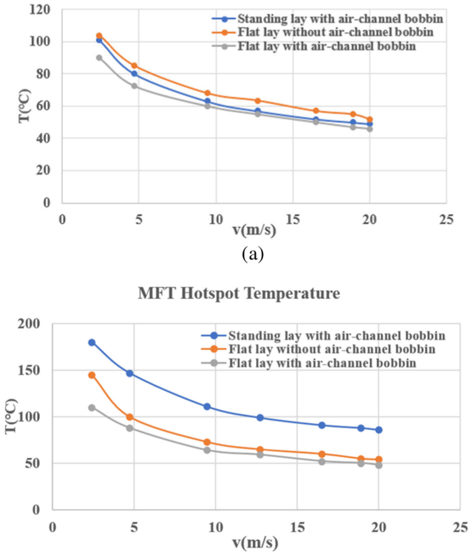

(a)

(b)

Fig. 15. Hotspot temperatures under different airflow speeds. (a) Core hotspot temperature. (b) MFT hotspot temperature.

F. Insulation Design

For the parallel-concentric winding structure, the well-coupled layout of the primary and secondary windings creates a challenge for achieving good electrical insulation [40]. To address this issue, a novel insulation structure is proposed, which utilizes two 3-D printed bobbin layers separated by an air channel. To keep enough clearance distance between inner-layer windings and outer-layer windings, a two-layer bobbin structure

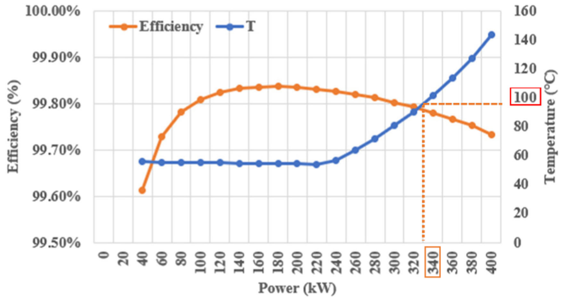

Fig. 16. MFT efficiency and hotspot temperature estimation.

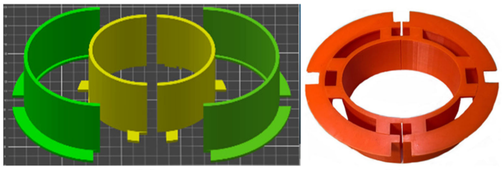

(a) (b)

Fig. 17. 3-D printed bobbin. (a) 3-D model. (b) 3-D printed bobbin prototype.

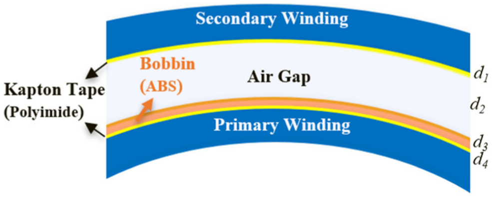

Fig. 18. Zoomed-in insulation structure between primary winding and secondary winding.

is designed. Fig. 17(a) shows the 3-D model of the two layers of bobbin design in the MFT. As shown in Fig. 17(b), the 3-D printed bobbin prototype uses acrylonitrile butadiene styrene (ABS) as insulation material. The 3-D printer can achieve a 0.4-mm accuracy.

Fig. 18 shows the insulation structure between primary and secondary windings, which includes bobbin, air gap, and two layers of insulation tape. The electric fields distribution can be estimated as

$$U = d_1 E_{\text{tape\_sec}} + d_2 E_{\text{air}} + d_3 E_{\text{bobbin}} + d_4 E_{\text{tape\_pri}} \quad (10)$$

where U is voltage between primary and secondary winding, $E_{\text{tape\_pri}}$ and d_1 are, respectively, the electric field and thickness of primary winding insulation tape, E_{air} and d_2, respectively, the electric field and thickness of air gap, E_{bobbin} and d_3, respectively, the electric field and thickness of inner-layer bobbin, $E_{\text{tape\_sec}}$ and d_4 are, respectively, the electric field and thickness of secondary winding insulation tape. Under bipolar PWM excitation, the boundary condition for the normal field component across a medium interface is shown as follows:

$$\epsilon_{\text{tape}} E_{\text{tape\_sec}} = \epsilon_{\text{air}} E_{\text{air}} \quad (11)$$

$$\epsilon_{\text{air}} E_{\text{air}} = \epsilon_{\text{bobbin}} E_{\text{bobbin}} \quad (12)$$

$$\epsilon_{\text{bobbin}} E_{\text{bobbin}} = \epsilon_{\text{tape}} E_{\text{tape\_pri}} \quad (13)$$

TABLE VII
TRANSFORMER INSULATION DESIGN PARAMETERS

	Thickness (mm)	Material	Dielectric Strength@25 °C	Dielectric Constant	Thermal Conductivity
Bobbin	3	Acrylonitrile Butadiene Styrene (ABS)	16.7 kV/mm	2.87	0.17 W/mK
Insulation Tape	0.05	polyimide	102 kV/mm	3.5	0.12 W/mK

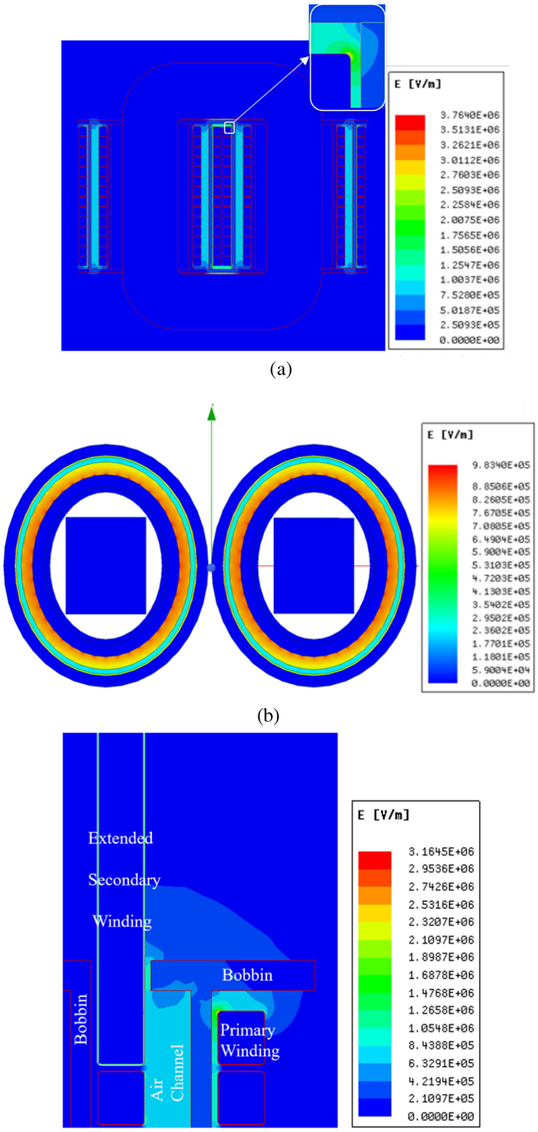

(a)

(b)

(c)

Fig. 19. Maxwell 2-D electrostatic simulation under applied voltage of 7.5 kV. (a) Electric field of front view. (b) Electric field of top view. (c) Electric field of extended inner winding.

where ϵ_{air} and ϵ_{bobbin} are, respectively, the dielectric constants of air and bobbin material, and ϵ_{tape} is dielectric constants of winding insulation tape. The main parameters of insulation materials used in the design are shown in Table VII. Based on the abovementioned insulation design, a 2-D model is constructed to simulate the electric field distribution in the MFT, as shown in Fig. 19.

According to the IEEE Std. C57.12.01 Standard [41], 7.5 kV is applied between the primary and secondary windings in the simulation. Fig. 19(a) shows the maximum electric field is at the top and bottom windings because of the relatively small distance to the magnetic core. The thermal-shrinkage tube is used for top and bottom windings to insulation capability. The longest air gap between the inner-layer and outer-layer bobbin is 19 mm in the y-axis direction and the shortest air distance is 18 mm in the x-axis direction. As shown in Fig. 19(b), the area between the inner layer and outer layer in the x-axis direction has a higher electric field. Fig. 19(c) indicates that electric filed strength increases due to the extended secondary winding, but still in accept range because of enough clearance and creepage distance here. At ambient pressure, the air breakdown field (PD inception field) is around 3 kV/mm, which could be roughly estimated based on the element geometry and Paschen's law. The simulation results suggest that the electric field at working voltage is well below the air breakdown field, which indicates that no significant PD is expected to be observed at this voltage level.

Since the MFT is operating under bipolar PWM excitation in the DAB converter, the electric field in the air and dielectric is capacitively determined. The field strength in the air gap or gas-filled void is typically higher than that in the solid dielectric. Thus, the air gap is usually the weakest element in the insulation chain. To remove PDs from air gaps, the field strength in the air gap should be less than a certain threshold, which is determined by the MFT configuration. More fundamentally, the threshold or the PD inception field in air gap could be roughly estimated by the Paschen's law. Thus, one way to increase the PD inception voltage (PDIV) of the MFT is to increase the thickness of the air gap. Ideally, a large air gap between primary and secondary windings would significantly increase the MFT PDIV. However, there is a clear space limitation due to the power density requirement of the MFT as well as the leakage inductance requirement. To achieve desired power density as well as thermal and efficiency performance, the size of the MFT needs to be limited. Thus, an optimal air gap between the primary and secondary windings needs to be selected to achieve a high PDIV level for the MFT while minimizing the losses and size.

IV. OPTIMIZATION

In this article, an optimal design methodology is developed to maximize the efficiency while satisfying all the design boundary conditions. The boundary conditions include magnetic core dimension limitation, electrical insulation requirements, and hot-spot temperature limitation. Based the modeling of core losses, winding losses, and electric field distribution, the MFT efficiency and maximum electric field strength can be express as a function of the parameters in the optimization flow chart.

The optimization methodology consists of predesign, preliminary design, and optimal design. The three-stage optimization helps to improve the design efficiency and feasibility. Moreover, by leveraging the advantage of 3-D printing technology, more optimal design freedoms and accurate fabrication can be achieved.

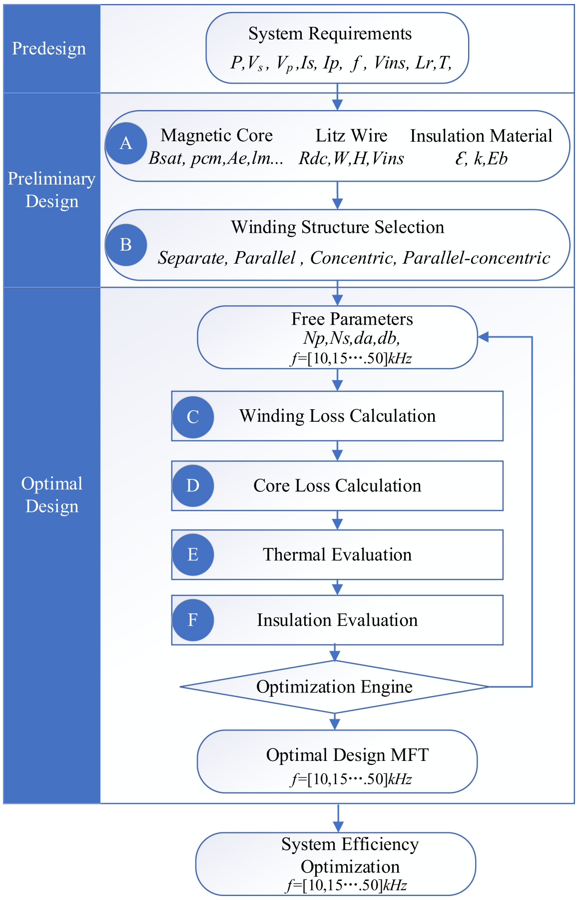

Fig. 20. MFT design optimization flowchart.

Fig. 20 shows the proposed MFT optimization flowchart. Predesign stage covers the system-level requirements, which include output power (P), operating frequency (f), input voltage (V_p), output voltage (V_s), leakage inductance (L_r), insulation requirement (V_{ins}), and temperature rise limitation (T).

Most of the parameters in this stage are selected by system requirements. The preliminary design stage decides the magnetic core material (B_{sat}, P_{cm}) and dimension (A_e, l_m), Litz wire type (R_{dc}, W, H), insulation materials (ε, k, E_b), and winding structure. This step is the foundation of the optimal design and has relatively less flexibility because of the limited number of commercial products. The parameters in this stage are compared and analyzed to achieve high efficiency and high insulation MFT design.

The optimal design stage starts with defining free parameters. In the optimization, the switching frequency f is swept from 10 to 50 kHz. Each frequency has its own optimal design. In total, 15 kHz is selected which is based on the efficiency and dimension optimization of the whole DAB converter system. Turns number Np and Ns are important parameters due to the close relationship with flux density and insulation. Bobbin dimension (da, db) is another key parameter in MFT design. Bobbins provide mechanical support for winding and cores, create airflow channels for cooling, and change the electrical field distribution. Inner-layer bobbin dimensions are fixed to

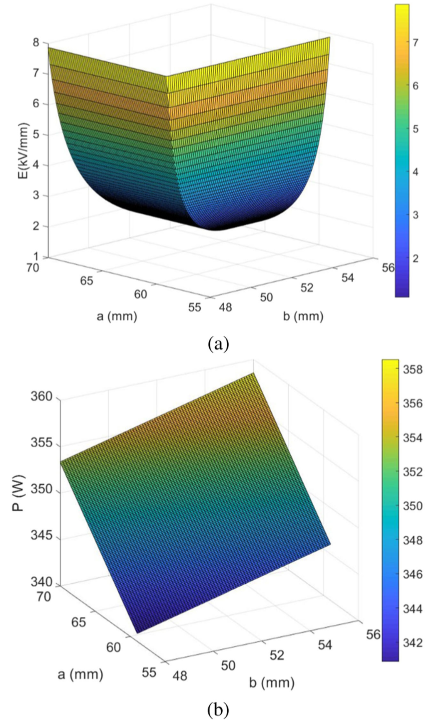

(a)

(b)

Fig. 21. (a) Electrical distribution in *xy* plane versus outer-layer bobbin dimension. (b) MFT losses versus outer-layer bobbin dimension at turns ratio 14:14.

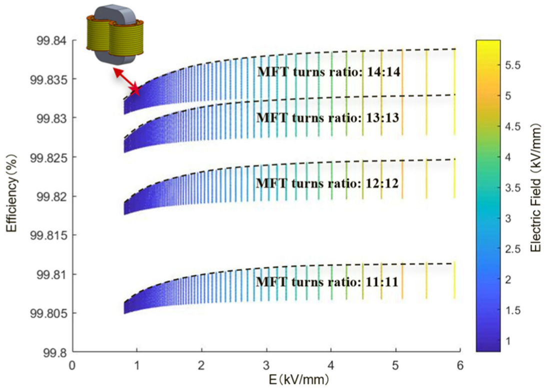

Fig. 22. Efficiency versus maximum electric field of feasible MFTs according to the proposed design methodology.

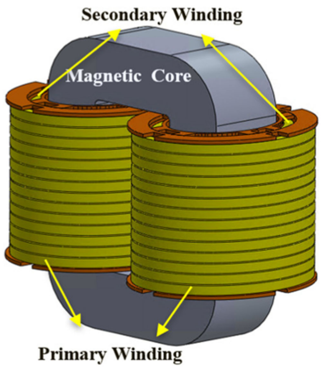

Fig. 23. 3-D model of the high-power (200 kW) MFT prototype.

TABLE VIII
TRANSFORMER PROTOTYPES DESIGN PARAMETERS

Parameters	Values
Operating Frequency (*fs*)	15kHZ
Core Material	FINEMET® FT-3TL x 2
Litz wire Stand number /AWG	4000/40
Turn Number(*N*)	14:14
Leakage /Magnetizing inductance (Lr/Lm)	5.36 µH / 21.67 mH (0.0247%)
Dimension (L/W/H)	258 mm / 168 mm / 240 mm

match the magnetic core. Fig. 21(a) shows the relationship of electrical distribution in the *xy* plane with semiminor axis *b* and semimajor axis *a* of outer-layer ellipse bobbin. The smaller value of *a* and *b* means the smaller clearance and creepage distance between primary and secondary windings. Fig. 21(b) shows the relationship of MFT losses with semiminor axis *b* and semimajor axis *a* of outer-layer ellipse bobbin at 14:14 turns ratio. The core loss is fixed and winding loss changes with bobbin dimension.

The number of turns and dimensions of bobbins is swept over an available range. Each set of free parameters corresponds to a complete MFT design. These sets of free parameters are then applied to the design flowchart shown in Fig. 20 to find the optimal design. Fig. 22 shows all the swept results with different turns number. The optimization is a tradeoff between efficiency and maximum electric field. Considering the fabrication error and extreme insulation cases, the final optimization MFT design is highlighted in Fig. 22 with the red star. According to the MFT optimization result, it is expected to reach a power density of 19.3 kW/L and the efficiency of 99.842% at 200 kW.

V. MFT PROTOTYPE AND EXPERIMENTAL VERIFICATION

A. *Transformer Prototype and Key Parameters*

Based on the specifications list in Table II and optimal design procedure discussed earlier, a high-power MFT prototype with two FINEMET FT-3TL magnetic cores and parallel-concentric winding structure is developed, as shown in Fig. 23. Table VIII shows the MFT prototype key parameters, it achieves extremely low-leakage inductance to magnetizing inductance ratio (0.0247%).

B. *PD Test*

To achieve sufficient insulation design, the electric field in each insulation layer needs to be less than a threshold to ensure that the insulation system can achieve the desired lifetime. In addition, PD needs to be removed during the design stage, since the internal PD may degrade insulation material during normal operation and cause premature failure for the MFT. Thus, it is crucial to investigate if the MFT is suffering from PD at the rated voltage level. For the MFT, the voltage excitation should be bipolar PWM waveform. However, there is no well-established standard method to reliably conduct PD measurement under PWM excitations. The Litz wire windings of MFT have been tested with 10 kHz bipolar PWM waveforms by a new developed prototype. To make sure the selected Litz wire and insulation components PD free at working voltage.

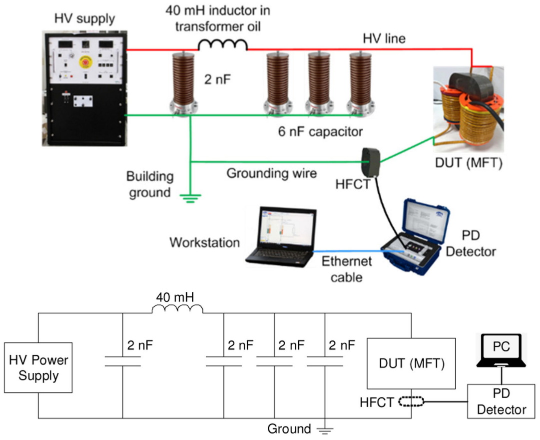

Fig. 24. Circuit diagram of the PD test platform.

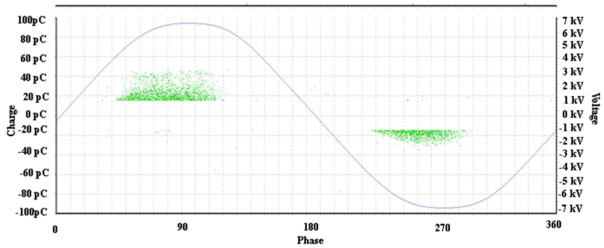

Fig. 25. PD pattern diagram at ac 60 Hz 7.5 kV peak (5-min test data).

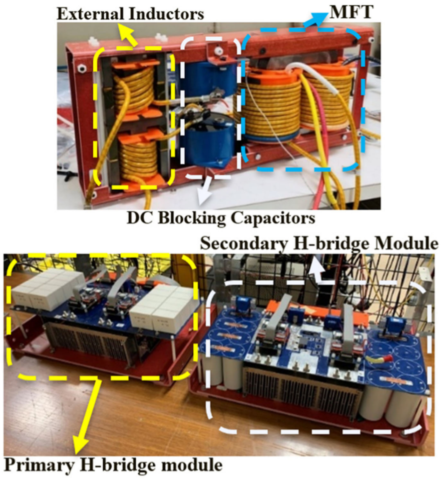

Fig. 26. 200-kW DAB converter hardware.

Besides, since the article is focusing on PD detection, a 60 Hz sine wave voltage is adapted to perform the PD detection for the developed MFTs. This PD detection is based on IEC 60270 [42], which has been widely used in power industry and proved to be a reliable way for PD detection.

The circuit diagram of the PD test setup is shown in Fig. 24. High-frequency current transformer is used to capture the PD impulse current. A C-L-3C filter is designed to remove the noise from the power supply. As all interconnections are properly terminated, this setup can conduct both ac and dc PD tests up to 30 kV with a background noise level of 5 pC. Fig. 25 shows the pattern diagram of the PD test at ac 60 Hz excitation and

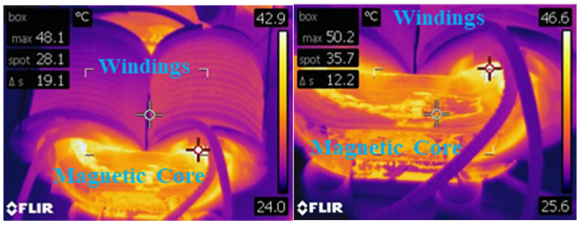

Fig. 27. Thermal camera image of the MFT steady state at 15 kHz and 200 kW output power.

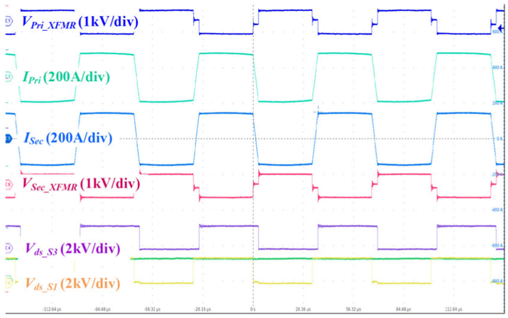

Fig. 28. Experimental waveforms of MFT at 15 kHz and output power 200 kW.

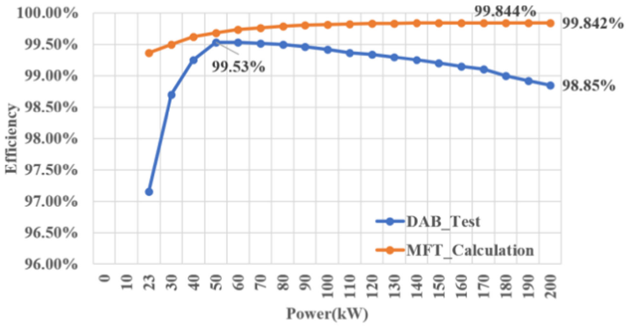

Fig. 29. Measured DAB converter efficiency and MFT efficiency.

the measured PDIV is around 5.3 kV rms/7.5 kV peak, which is an averaged value over multiple tests. PD pattern diagram at ac 60 Hz 7.5 kV peak shows all the PD smaller than 50 pC of IEEE Standard requirements. In addition, the PD rate is much less than 1 pulse/cycle.

C. DAB Experimental Test

A 200 kW DAB converter is developed with the high-power MFT, as shown in Fig. 26. The prototype transformer is tested at 1300 V input voltage and 15 kHz operating frequency with the DAB converter. In total, 1700 V SiC MOSFET half-bridge modules are used as the power switches. The steady-state thermal performance of the MFT at 200 kW power rating with air cooling was measured and shown in Fig. 27. The measured maximum surface temperature rise of the core is around 25 °C and winding temperature rise is 23 °C. Fig. 28 shows the experimental waveforms of the MFT primary current and secondary voltage at 200 kW. Fig. 29 shows the overall conversion efficiency of the DAB and MFT up to 200 kW. The DAB efficiency is captured by HIOKI PW6001 power analyzer with a calibrated current sensor and voltage sensor. The peak efficiency of the DAB converter is 99.53% at 50 kW, and the efficiency at 200 kW is 98.85%. The MFT efficiency is calculation efficiency based on experimental core losses and winding losses information. Besides, the MFT core losses were verified by FEA simulation and winding losses was verified by the Dowell model. The peak efficiency of the MFT is 99.844% at around 180 kW, and the efficiency at 200 kW is 99.842%.

VI. CONCLUSION

The optimal design of the MFT is a complex tradeoff process. Comparison and selection of various materials and structures according to the specific converter applications are needed. Besides, basic parameters measurement and tests such as ac resistance, core losses test, and PD test are essential during the design process.

This article presents a 200 kW MFT optimal design methodology and experimental test results. The proposed optimal design methodology consists of predesign, preliminary design, and optimal design. By leveraging the advantage of the 3-D print technology, more optimal design freedoms and accurate fabrication can be achieved. To verify the effectiveness of the design, a 200 kW, 15 kHz MFT prototype was developed. Insulation between primary and secondary windings has been successfully tested at 12 kV ac peak voltage, and the design is PD free up to 5.3 kV rms. The prototyped MFT had been successfully used in a 200 kW DAB converter, achieving a peak efficiency of 99.53% at 50 kW and an efficiency of 98.85% at 200 kW. These results are the highest efficiency ever reported for converters at this power level. The peak efficiency of MFT is estimated to be 99.844% at 180 kW, and 99.842% at 200 kW. The temperature rise of the MFT core at 200 kW is lower than 30 °C, which means that this MFT prototype can operate at an even higher power level.

REFERENCES

[1] S. M. Tayebi, W. Xu, H. Wang, R. Yu, Z. Guo, and A. Q. Huang, "A single-stage isolated resonant SiC DC/AC inverter for efficient high-power applications," in *Proc. IEEE Appl. Power Electron. Conf. Expo.*, 2020, pp. 399–404.

[2] Y. Du, S. Baek, S. Bhattacharya, and A. Q. Huang, "High-voltage high frequency *transformer* design for a 7.2 kv to 120 v/240 v 20 kva solid state transformer," in *Proc. 36th Annu. Conf. IEEE Ind. Electron. Soc.*, Nov. 2010, pp. 493–498.

[3] W. A. Roshen, "A practical, accurate and very general core loss model for non-sinusoidal waveforms," *IEEE Trans. Power Electron.*, vol. 22, no. 1, pp. 30–40, Jan. 2007.

[4] M. A. Bahmani, T. Thiringer, and H. Ortega, "An accurate pseudo empirical model of winding loss calculation in hf foil and round conductors in switch mode magnetics," *IEEE Trans. Power Electron.*, vol. 29, no. 8, pp. 4231–4246, Aug. 2014.

[5] P. Shuai and J. Biela, "Design and optimization of medium frequency, medium voltage transformers," in *Proc. 15th Eur. Conf. Power Electron. Appl.*, 2013, pp. 1–10.

[6] S. Zhao, Q. Li, and F. Lee, "High frequency transformer design for modular power conversion from medium voltage AC to 400 v dC," in *Proc. Appl. Power Electron. Conf. Expo.*, Mar. 2017, pp. 2894–2901.

[7] L. Heinemann, "An actively cooled high power, high frequency transformer with high insulation capability," in *Proc. APEC 17th Annu. IEEE Appl. Power Electron. Conf. Expo.*, Mar. 2002, pp. 352–357.

[8] C. Zhao *et al.*, "Power electronic traction transformer—Medium voltage prototype," *IEEE Trans. Ind. Electron.*, vol. 61, no. 7, pp. 3257–3268, Jul. 2014.

[9] G. Ortiz, M. Leibl, J. W. Kolar, and O. Apeldoorn "Medium frequency transformer for solid-state-transformer application-design and experimental verification," in *Proc. IEEE 10th Int. Conf. Power Electron. Drive Syst.,* 2013, pp. 1285–1290.

[10] G. Ortiz, M. G. Leibl, J. E. Huber, and J. W. Kolar, "Design and experimental testing of a resonant DC–DC converter for solid-state transformers," *IEEE Trans. Power Electron.,* vol. 32, no. 10, pp. 7534–7542, Oct. 2017.

[11] M. A. Bahmani, T. Thiringer, and M. Kharezy, "Optimization and experimental validation of medium-frequency high power transformers in solid-state transformer applications," in *Proc. Annu. IEEE Appl. Power Electron. Conf. Expo.*, 2016, pp. 3043–3050.

[12] M. Mogorovic and D. Dujic, "100 kW, 10 kHz medium frequency transformer design optimization and experimental verification," *IEEE Trans. Power Electron*, vol. 34, no. 2, pp. 1696–1708, Feb. 2019.

[13] T. Gradinger, U. Drofenik, and S. Alvarez, "Novel insulation concept for an mv dry-cast medium-frequency transformer," in *Proc. 19th Eur. Conf. Power Electron. Appl.*, 2017, pp. 1–10.

[14] S. Isler, T. Chaudhuri, D. Aguglia, and X. A. Bonnin, "Development of a 100 kW, 12.5 kV, 22 kHz and 30 kV insulated medium frequency transformer for compact and reliable medium voltage power conversion," in *Proc. 19th Eur. Conf. Power Electron. Appl. (EPE'17 ECCE Europe)*, Warsaw, 2017, pp. P.1–P.10, doi: 10.23919/EPE17ECCEEurope.2017.8099196.

[15] A. Garcia-Bediaga, I. Villar, A. Rujas, L. Mir, and A. Rufer, "Multiobjective optimization of medium-frequency transformers for isolated soft-switching converters using a genetic algorithm," *IEEE Trans. Power Electron.*, vol. 32, no. 4, pp. 2995–3006, Apr. 2017.

[16] P. Huang *et al.*, "Optimal design and implementation of high-voltage high-power silicon steel core medium-frequency transformer," *IEEE Trans. Ind. Electron.*, vol. 64, no. 6, pp. 4391–4401, Jun. 2017.

[17] X. She, X. Yu, F. Wang, and A. Q. Huang, "Design and demonstration of a 3.6-kV–120-V/10-kVA solid-state transformer for smart grid application," *IEEE Trans. Power Electron.*, vol. 29, no. 8, pp. 3982–3996, Aug. 2014.

[18] T. Zhao, G. Wang, S. Bhattacharya, and A. Q. Huang, "Voltage and power balance control for a cascaded H-Bridge converter-based solid-state transformer," *IEEE Trans. Power Electron.*, vol. 28, no. 4, pp. 1523–1532, Apr. 2013.

[19] H. Akagi, S. I. Kinouchi, and Y. Miyazaki, "Bidirectional isolated dual active-bridge (DAB) DC-DC converters using vol. 1.2-kV 400-A SiC MOSFET dual modules," *CPSS Trans. Power Electron. Appl.*, vol. 1, no. 1, pp. 33–40, Dec. 2016.

[20] W. Xu *et al.*, "Hardware design and demonstration of a 100kW, 99% efficiency dual active half bridge converter based on 1700V SiC power MOSFET," in *Proc. IEEE Appl. Power Electron. Conf. Expo.*, 2020, pp. 1367–1373.

[21] W. Xu, R. Yu, Z. Guo, and A. Q. Huang, "Design of 1500V/200kW 99.6% efficiency dual active bridge converters based on 1700V SiC power MOSFET module," in *Proc. IEEE Energy Convers. Congr. Expo.*, 2020, pp. 6000–6007.

[22] W. A. Roshen, "A practical, accurate and very general core loss model for non-sinusoidal waveforms," *IEEE Trans. Power Electron.*, vol. 22, no. 1, pp. 30–40, Jan. 2007.

[23] F. Krismer and J. W. Kolar, "Accurate power loss model derivation of a high-current dual active bridge converter for an automotive application," *IEEE Trans. Ind. Electron.*, vol. 57, no. 3, pp. 881–891, Mar. 2010.

[24] D. Dujic, F. Kieferndorf, F. Canales, and U. Drofenik, "Power electronic traction transformer technology—An overview," in *Proc. 7th Int. Power Electron. Motion Control Conf.*, 2012, pp. 636–642.

[25] *FINEMET FT-3TL F/RT Series Core*, Hitachi Metals, Ltd., Tokyo, Japan, T-YT3 May 2014.

[26] P. Shuai and J. Biela, "Investigation of acoustic noise sources in medium frequency, medium voltage transformers," in *Proc. 16th Eur. Conf. Power Electron. Appl.*, 2014, pp. 1–11.

[27] C. W. T. McLyman, *Transformer and Inductor Design Handbook*, 3rd ed. Boca Raton, FL, USA: CRC Press, Mar. 2004.

[28] J. Mühlethaler, J. W. Kolar and A. Ecklebe, "Loss modeling of inductive components employed in power electronic systems," in *Proc. 8th Int. Conf. Power Electron.* - ECCE Asia, Jeju, Korea (South), 2011, pp. 945–-952, doi: 10.1109/ICPE.2011.5944652.

[29] I. Villar, U. Viscarret, I. Etxeberria-Otadui, and A. Rufer, "Global loss evaluation methods for nonsinusoidally fed medium-frequency power transformers," *IEEE Trans. Ind. Electron.*, vol. 56, no. 10, pp. 4132–4140, Oct. 2009.

[30] C. P. Steinmetz, "A steinmetz contribution to the AC power evolution," *Proc. IEEE*, vol. 72, no. 2, pp. 196–197, Feb. 1984.

[31] J. Reinert, A. Brockmeyer, and R. W. A. A. De Doncker, "Accurate calculation of losses in ferro- and ferrimagnetic materials based on the modified Steinmetz equation," *IEEE Trans. Ind. Appl.*, vol. 37, no. 4, pp. 1055–1060, Jul./Aug. 2001.

[32] J. Li, T. Abdallah, and C. R. Sullivan, "Improved calculation of core loss with nonsinusoidal waveforms," in *Conf. Rec. 36th IEEE IAS Annu. Meeting*, Sep. 30, Oct. 4, 2001, pp. 2203–2210.

[33] K. Venkatachalam, C. R. Sullivan, T. Abdallah, and H. Tacca, "Accurate prediction of ferrite cores loss with nonsinusoidal waveforms using only steinmetz parameters," in *Proc. IEEE Workshop Comput. Power Electron.*, Jun. 3–4, 2002, pp. 36–41.

[34] HECTOR ORTEGA JIMENEZ, "AC resistance evaluation of foil, round and litz conductors in magnetic components," Department of Energy and Environment Master Thesis, Chalmers Univ. Technol., Goteborg, Sweden, 2013.

[35] P. Dowell, "Effect of eddy currents in transformers windings.," *Proc. Inst. Elect. Engineers*, vol. 113, no. 8, pp. 1387–1394, 1966.

[36] W. G. Hurley, E. Gath, and J. G. Breslin, "Optimizing the ac resistance of multilayer transformer windings with arbitrary current waveforms," *IEEE Trans. Power Electron.*, vol. 15, no. 2, pp. 369–376, Mar. 2000.

[37] R. Agarwal, S. Martin, Y. Shi, and H. Li, "High frequency transformer design for medium voltage shipboard DC-DC converter," in *Proc. IEEE Elect. Ship Technol. Symp.*, 2019, pp. 499–504.

[38] Convection from a Rectangular Plate, 2016. [Online]. Available: http://people.csail.mit.edu/jaffer/SimRoof/Convection/

[39] M. Fakoor-Pakdaman, M. Andisheh-Tadbir, and M. Bahrami, "Transient internal forced convection under arbitrary time-dependent heat flux," in *Proc. ASME Summer Heat Transfer Conf.*, Jul. 14–19, 2013.

[40] Z. Guo, S. Sen, S. Rajendran, Q. Huang, X. Feng, and A. Q. Huang, "Design of a 200 kW medium-frequency transformer (MFT) with high insulation capability," in *Proc. IEEE Energy Convers. Congr. Expo.*, 2020, pp. 3471–3477.

[41] *IEEE Standard for General Requirements for Dry-Type Distribution and Power Transformers*, IEEE Standard C57,12.01-2015, 2015.

[42] *International Standard IEC 60270*. High Voltage Test Techniques Partial Discharge Measurements, 3rd ed. International Electrotechnical Commission; Geneva, Switzerland, 2000.

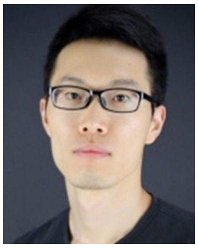

Zhicheng Guo (Student Member, IEEE) was born in Suzhou, China. He received the B.Sc. degree from Southeast University, Nanjing, China, in 2013, and the M.S. degree from National Tsing Hua University, Hsinchu, Taiwan, in 2016. He is currently working toward the Ph.D. degree with the Semiconductor Power Electronics Center, The University of Texas at Austin, Austin, TX, USA.

His research interests include the high-power magnetic design and power module packaging.

Ruiyang Yu (Member, IEEE) received the B.E. degree in electrical engineering from Shandong University, Jinan, China, in 2007, and the M.S. and Ph.D. degrees in power electronics from The University of Hong Kong, Hong Kong, in 2008 and 2013, respectively.

He was a Postdoctoral Research Fellow from 2013 to 2017 and an Instructor in 2016 with the North Carolina State University, Raleigh, NC, USA. He is currently a Research Associate with The University of Texas at Austin, Austin, TX, USA. His research interests include high-frequency and high-power-density power converter design, megawatt power converter design, magnetic components, and power converter control.

Wei Xu (Student Member, IEEE) received the B.S and M.S. degrees in electrical engineering from the Anhui University of Technology, Anhui, China, in 2011, and the Nanjing University of Aeronautics and Astronautics, Nanjing, China, in 2014. He is currently working toward the Ph.D. degree with The University of Texas at Austin, Austin, TX, USA.

He was a Senior Hardware Engineer from 2014 to 2018 with the High-Power Research Team (HPRT), DELTA Electronics, Shanghai, China. His research interests include high power, high frequency and high-density power converters, magnetic component designs, and power converter control.

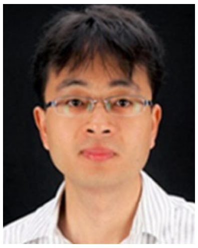

Xianyong Feng (Member, IEEE) received the Ph.D. degree in electric power engineering from the Department of Electrical and Computer Engineering, Texas A&M University, College Station, TX, USA, in 2012.

He is currently with the Center for Electromechanics, University of Texas at Austin, Austin, TX, USA. He was also with the ABB, Raleigh, NC, USA, and ExxonMobil, Houston, TX, USA. His research interests include the areas of microgrids, shipboard power systems, and dc power system protection.

Alex Q. Huang (Fellow, IEEE) was born in Zunyi, Guizhou, China. He received the B.Sc. degree in electrical engineering from Zhejiang University, Hangzhou, China, in 1983, and the M.Sc. degree in electrical engineering from Chengdu Institute of Radio Engineering, Chengdu, China, in 1986, and the Ph.D. degree from Cambridge University, Cambridge, U.K., in 1992.

From 1992 to 1994, he was a Research Fellow with the Magdalene College, Cambridge, U.K. From 1994 to 2004, he was a Professor with the Bradley Department of Electrical and Computer Engineering, Virginia Polytechnic Institute and State University, Blacksburg, VA, USA. From 2004 to 2017, he was the Progress Energy Distinguished Professor of Electrical and Computer Engineering with the NC State University, Raleigh, NC, USA, where he established and led the NSF FREEDM Systems Center. Since 2017, he has been the Dula D. Cockrell Centennial Chair in Engineering with the University of Texas at Austin, Austin, TX, USA. Since 1983, he has been involved in the development of modern power semiconductor devices and power integrated circuits. He fabricated the first IGBT power device in China in 1985. He is the Inventor and Key Developer of the emitter turn-OFF (ETO) thyristor. He developed the concept of energy Internet and the smart-transformer-based energy router technology. His current research interests include power electronics, power management microsystems, and power semiconductor devices. He has mentored and graduated more than 80 Ph.D. and master students, and has authored or coauthored more than 500 papers in international conferences and journals. He has also been granted more than 20 U.S. patents.

Dr. Huang is the recipient of the NSF CAREER Award, the prestigious R&D 100 Award, the MIT Technology Review's 2011 Technology of the Year Award, and the 2019 IEEE IAS Gerald Kliman Innovator Award. He is a fellow of National Academy of Inventors.